Series-Resonant VHF Micromechanical Resonator Reference Oscillators

Yu-Wei Lin, *Student Member, IEEE*, Seungbae Lee, *Student Member, IEEE*, Sheng-Shian Li, *Student Member, IEEE*, Yuan Xie, *Student Member, IEEE*, Zeying Ren, *Member, IEEE*, and Clark T.-C. Nguyen, *Senior Member, IEEE*

***Abstract*—Series-resonant vibrating micromechanical resonator oscillators are demonstrated using a custom-designed single-stage zero-phase-shift sustaining amplifier together with planar-processed micromechanical resonator variants with quality factors Q in the thousands that differ mainly in their power-handling capacities. The resonator variants include two 40-μm-long 10-MHz clamped-clamped-beam (CC-beam) resonators, one of them much wider than the other so as to allow larger power-handling capacity, and a 64-μm-diameter 60-MHz disk resonator that maximizes both Q and power handling among the resonators tested. Tradeoffs between Q and power handling are seen to be most important in setting the close-to-carrier and far-from-carrier phase noise behavior of each oscillator, although such parameters as resonant frequency and motional resistance are also important. With a 10$\times$ higher power handling capability than the wide-width CC-beam resonator, a comparable series motional resistance, and a 45$\times$ higher Q of 48 000, the 60-MHz wine glass resonator reference oscillator exhibits a measured phase noise of -110 dBc/Hz at 1-kHz offset, and -132 dBc/Hz at far-from-carrier offsets. Dividing down to 10 MHz for fair comparison with a common conventional standard, this oscillator achieves a phase noise of -125 dBc/Hz at 1-kHz offset, and -147 dBc/Hz at far-from-carrier offsets.**

***Index Terms*—Gain control, microelectromechanical devices, microresonators, nonlinear distortion, oscillator noise, oscillators, phase noise, resonators.**

I. Introduction

RECENT interest in tiny or ultrathin wireless applications, such as wireless microsensors [1], [2] and credit-card-sized wireless devices, have fueled efforts to flatten the form factors of the off-chip passives needed for filtering and frequency generation in wireless communication circuits. Among off-chip components in a wireless communication transceiver, the quartz crystal used in the reference oscillator is perhaps the most difficult to miniaturize and integrate on chip, since on-chip devices capable of matching its quality factor Q (on the order of 10 000) and temperature stability (better than 35 ppm uncompensated over 0 °C–70 °C) have so far been unavailable. In particular, the on-chip electrical resonators provided by conventional integrated circuit (IC) technologies, such as spiral LC tanks and active biquads, generally post Qs no larger than 10 [3] in the frequency range of interest. Even more exotic technologies that lift inductors out of the plane of the substrate still achieve Qs no larger than 85 [4], which is impressive, but nowhere near the >1000 required for reference oscillator phase noise and temperature stability specifications. Inevitably, losses from series resistance, substrate coupling, and parasitic capacitance, end up limiting the Qs of electrical resonators to values much smaller than those exhibited by vibrating mechanical counterparts, such as quartz crystals, for which losses through gas damping and intrinsic material damping comprise a much smaller percentage of the total energy per cycle, allowing for orders of magnitude higher Q.

For this reason, recent efforts to miniaturize and integrate the reference oscillator function have focused on micromachined vibrating resonators as potential replacements for the high Q and temperature stable, but bulky, quartz crystals that presently govern reference oscillator phase noise performance, temperature stability, and frequency accuracy. Among the most promising of these vibrating micromechanical resonators are capacitively transduced surface-micromachined polysilicon beam and disk resonators with Qs exceeding 145 000 in vacuum [5], [6], thin-film bulk acoustic piezoelectric resonators (FBARs) with Qs up to 2500 [7], and capacitively transduced single-crystal silicon resonators [8] with Qs up to 130 000 when operating in a square-extensional mode [9]. Hybrid oscillators based on each of the above resonator types have been demonstrated recently [10]–[14], with only the last of these meeting the GSM reference oscillator phase noise performance specifications (of -130 dBc/Hz at 1-kHz offset from a 13-MHz carrier and -150 dBc/Hz at far-from-carrier offsets) using an off-the-shelf amplifier. None of these oscillators come close to the required temperature dependence specifications of less than 2 ppm total frequency shift from 0 °C–70 °C after compensation.

To address the temperature stability issue, an on-chip vibrating capacitively transduced clamped–clamped beam (CC-beam) micromechanical resonator based on MEMS surface-micromachining technology was recently demonstrated at 10 MHz with a Q of 4000 and a frequency stability of 18 ppm over 0 °C–80 °C [15], which is better than most cuts of AT quartz [16], and which now provides a potential path toward a fully integrated communications reference oscillator. This, together with recent demonstrations of polysilicon micromechanical resonators in the gigahertz range with Qs still larger than 10 000 [17]–[20], even when operating in air, and a proven ability for full on-chip planar integration with transistors [21], makes capacitively transduced surface-micromachined vibrating resonators attractive candidates for both filtering and oscillator functions in wireless communication circuits.

Manuscript received June 1, 2004; revised July 10, 2004. This work was supported by the Defense Advanced Research Projects Agency (DARPA) under Grant F30602-01-1-0573.

The authors are with the Department of Electrical Engineering and Computer Science, University of Michigan, Ann Arbor, MI 48109-2122 USA (e-mail: ywlin@umich.edu; ctnguyen@umich.edu).

Digital Object Identifier 10.1109/JSSC.2004.837086

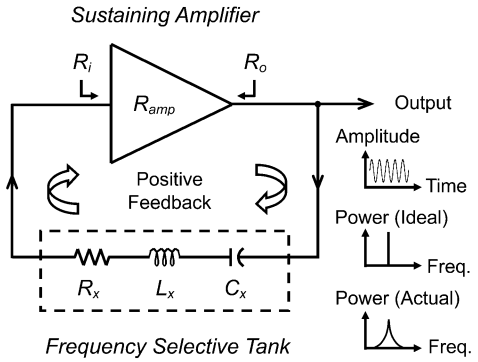

Fig. 1. General topology for a series-resonant oscillator.

Unfortunately, a recently demonstrated 10-MHz oscillator using a variant of the above CC-beam resonator together with an off-the-shelf amplifier exhibits a phase noise of only −80 dBc/Hz at 1-kHz carrier offset, and −116 dBc/Hz at far-from-carrier offsets [10]—inadequate values caused mainly by the insufficient power-handling ability of the CC-beam micromechanical resonator device used [22].

This work demonstrates the impact of micromechanical resonator power handling and Q on oscillator performance by assessing the performance of an oscillator comprised of a custom-designed sustaining transresistance amplifier IC together with three different capacitively transduced micromechanical resonators: a 10-MHz CC-beam similar to that in [10], a 10-MHz wide-width CC-beam with a 5× wider width for higher power handling; and a 60-MHz wine glass disk resonator with a 10× higher power handling capability than the wide-width CC-beam, a comparable series motional resistance, and a 45× higher Q of 48 000. The combination of the wine glass micromechanical disk resonator with the custom-IC CMOS transresistance sustaining amplifier yields a 60-MHz reference oscillator that achieves a phase noise density of −110 dBc/Hz at 1-kHz offset from the carrier, and −132 dBc/Hz at far-from-carrier offsets, while consuming only 350 μW of amplifier power, which is substantially lower than the milliwatts typically needed by the quartz crystal oscillators presently used in cellular telephones. Dividing down to 10 MHz for fair comparison, these values correspond to −125 dBc/Hz at 1-kHz offset from a 10-MHz carrier, and an effective −147 dBc/Hz far-from-carrier value. These values nearly satisfy or already satisfy (for some renditions) the reference oscillator specifications for wireless handsets. This, together with the potential for single-chip integration via any of several already demonstrated processes [21], [23], [24], [25], makes the micromechanical resonator oscillator of this work an attractive on-chip replacement for quartz crystal reference oscillators in communications and other applications.

II. Oscillator Design Tradeoffs: Q Versus Power Handling

Fig. 1 presents the top-level schematic of the oscillator circuit used in this work, where the micromechanical resonator is represented by an equivalent series *LCR* circuit to be specified later. As shown, a series resonant configuration is used, employing a transresistance sustaining amplifier in order to better accommodate the somewhat large motional resistance R_x, on the order of several kΩ, exhibited by some of the micromechanical resonators to be used. Here, the use of a transresistance amplifier with small input and output resistances effectively imposes a smaller load on the series resonator, allowing it to retain its very large Q. The conditions required for sustained oscillation can be stated as follows.

1) The gain of the transresistance sustaining amplifier $R_{\rm amp}$ should be larger than the sum of the micromechanical resonator's motional resistance, plus the input and output resistances of the sustaining amplifier, and any other sources of loss in the feedback loop, i.e.,

$$R_{\rm amp} \geq R_x + R_i + R_o = R_{\rm tot} \tag{1}$$

where $R_{\rm tot}$ is the total resistance that can consume power within the oscillation loop. In essence, this criterion states that the loop gain $A_l = (R_{\rm amp}/R_{\rm tot})$ must be greater than 1. At start-up, a loop gain of 3 or greater is recommended to insure oscillation growth, even in the face of process variations.

2) The total phase shift around the closed positive feedback loop must be 0°. In this series-resonant topology, an ideal situation exists when both the micromechanical resonator and transresistance sustaining amplifier have 0° phase shifts from input to output. In practice, there will be a finite amplifier phase shift, which can be minimized by choosing the amplifier bandwidth to be at least 10× greater than the oscillation frequency.

As the oscillation amplitude builds, nonlinearity in either the sustaining amplifier or the resonator tank reduces $R_{\rm amp}$ or raises $R_{\rm tot}$, respectively, until the loop gain equals unity, at which point the amplitude no longer grows and steady-state oscillation ensues. As will be seen, unlike quartz crystal oscillators, where the oscillation amplitude usually limits via amplifier nonlinearity, surface-micromachined micromechanical resonator oscillators without automatic level control (ALC) circuitry generally limit via nonlinearity in the micromechanical resonator [21].

Since the main function of a reference oscillator is to provide one and only one output frequency f_o, the output sinusoid of Fig. 1 should ideally be a delta function in the frequency domain, as shown in the figure. Given that an oscillator's output can be fundamentally modeled as noise filtered by an extremely high-Q filter, where the Q of the resonator tank is effectively amplified in the positive feedback loop to a value often more than 10^{10} times its stand-alone value [26], the output can be very close to a delta function if the initial resonator Q is large. However, since the resonator Q is not infinite, there will still be output power at frequencies adjacent to f_o. If the power at f_o (and only at f_o) is considered the desired output, then this adjacent "sideband" power is considered unwanted noise. If the oscillator amplitude is constant (which is generally true for the case of hard limiting or ALC), then amplitude noise is largely removed, and half of the total original noise power remains as phase noise [26].

Phase noise both close and far from the carrier are undesirable in reference oscillators used for wireless communications. In particular, close-to-carrier phase noise contributes directly to the system noise figure by adding noise inside the system bandwidth. Far-from-carrier phase noise undermines a receiver's ability to attenuate undesired adjacent channel signals. Again, the stringent GSM specification requires phase noise-to-carrier density ratios of -130 dBc/Hz at 1-kHz offset from a 13-MHz carrier, and -150 dBc/Hz at far-from-carrier offsets.

The single-sideband phase-noise density to carrier power ratio $L\{f_m\}$ at an offset frequency f_m from the carrier f_o of an oscillator can be computed by determining the transfer function of the described extremely high Q filter, sending the total system noise through its transfer function [26], and then interpreting all power at f_o as output power, and all other powers (at offsets f_m) as noise. Doing so for the series resonant oscillator of Fig. 1 yields an expression similar to Leeson's equation [27]

$$L\{f_m\} = \frac{2kT(1+F_{\text{Ramp}})}{P_o} \cdot \left(\frac{R_{\text{tot}}}{R_x}\right) \cdot \left[1 + \left(\frac{f_o}{2Q_l \cdot f_m}\right)^2\right] \tag{2}$$

where k is Boltzmann's constant, F_{Ramp} is the noise factor of the sustaining amplifier [21], Q_l is the loaded Q, given by

$$Q_l = \frac{R_x}{R_x + R_i + R_o} Q = \frac{R_x}{R_{\text{tot}}} Q \tag{3}$$

and $P_o = (1/2) i_o^2 R_{\text{tot}}$ is the oscillator signal power. From (2), the two most convenient methods to reduce phase noise are: 1) increase the loaded Q_l of the resonator tank and 2) increase the oscillation signal power P_o. As mentioned, increasing Q_l yields a more delta-function-like frequency response, and thus, reduces the noise at small offset frequencies from the carrier (i.e., close-to-carrier phase noise). On the other hand, from the first term in (2), increasing signal power increases the signal-to-noise ratio, thus improving the phase-noise performance. Although an increase in signal power reduces $L\{f_m\}$ at all carrier offsets, its influence is particularly important at large offset frequencies from the carrier (i.e., far-from-carrier phase noise), where noise from sources outside the feedback loop that are not shaped by the Q of the resonant tank element normally dominates.

III. Micromechanical Resonator Design

The four resonator attributes that most influence oscillator design and performance are its resonance frequency, series motional resistance, Q, and power-handling ability. In general, these parameters are strong functions of both the resonator geometry and the bias and excitation signals applied to it. Of these parameters, micromechanical resonators and quartz crystals differ the most in the power-handling category, where the much larger quartz crystals are capable of handling greater power without going nonlinear than their tiny micromechanical resonator counterparts. It is in fact the smaller power handling of micromechanical resonators that cause oscillators referenced to these devices to limit via resonator (rather than amplifier) nonlinearity, and that has prevented previous such oscillators [10] from achieving phase-noise performance values required by cellular wireless standards.

The following subsections detail the three micromechanical resonator designs compared in this work: a 10-MHz CC-beam similar to that in [10], a 10-MHz wide-width CC-beam, and a 60-MHz wine glass disk resonator, the design equations for each of which are summarized in Table I. In describing each design, these subsections illustrate the degree to which resonator geometry governs the four parameters that most strongly influence the performance of a micromechanical resonator oscillator.

A. CC-Beam Resonator

CC-beam micromechanical resonators [5] are among the most straightforward to design and implement. This, together with the simplicity of the three-mask polysilicon surface micromachining process used to fabricate them [5], makes them attractive for low-cost on-chip reference oscillator applications. Fig. 2 presents a perspective view schematic of a CC-beam resonator, together with a typical one-port bias and excitation scheme, and an equivalent electrical model. As shown, this device consists of a single beam suspended above a centrally located electrode and anchored to the substrate at its ends. To excite the CC-beam, a dc bias V_P is applied to the conductive beam, and an ac voltage v_i applied to its underlying electrode, where generally, $V_P \gg v_i$. (Note that there is no current flowing once the conductive structure is charged to V_P, so there is no dc power consumption.) This $V_P + v_i$ voltage combination generates a time-varying force that drives the beam into mechanical vibration when the frequency of v_i matches the beam resonance frequency f_o, given by [5]

$$f_o = 1.03 \cdot \kappa \cdot \sqrt{\frac{E}{\rho}} \cdot \frac{h}{L_r^2} \cdot \left[1 - \left(\frac{k_e}{k_m}\right)\right]^{\frac{1}{2}} \tag{4}$$

where E and ρ are the Young's modulus and density of the structural material, respectively, h and L_r are specified in Fig. 2, k_m and k_e are the purely mechanical and the electrical stiffness, respectively, and κ is a scaling factor that models the effect of surface topography [5]. To achieve a nominal resonance frequency of 10 MHz using a polysilicon structural material, for which $E = 150$ GPa and $\rho = 2300$ kg/m^3, some convenient micro-scale dimensions are $L_r = 40$ μm, $W_r = 8$ μm, and $h = 2$ μm. Note that these dimensions actually overshoot 10 MHz, but it is understood and assumed that the dc-bias-dependent electrical stiffness k_e will shift the frequency back.

Upon application of v_i at f_o, the ensuing resonance vibration creates a dc biased (by V_P) time-varying capacitance between the beam and its underlying electrode through which a motional current equal to

$$i_o = V_P \cdot \left|\frac{\partial C}{\partial x}\right| \cdot \frac{\partial x}{\partial t} \cong V_P \cdot \left(\frac{\varepsilon_o A_o}{d_o^2}\right) \cdot (\omega_o X) \tag{5}$$

can be generated and sensed at the output of this device, where $A_o = W_r W_e$ and d_o are the electrode-to-resonator overlap area and gap spacing, respectively, of the CC-beam resonator, $\partial C/\partial x$ is the change in resonator-to-electrode capacitance per unit displacement, X is the amplitude of vibration, $\omega_o = 2\pi f_o$

TABLE I
RESONATOR DESIGN EQUATION SUMMARY

	Clamped-Clamped Beam	Wine Glass Disk
Schematic	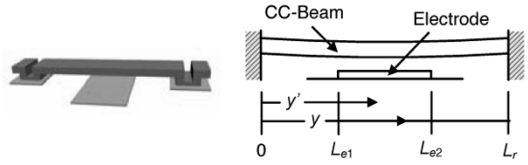	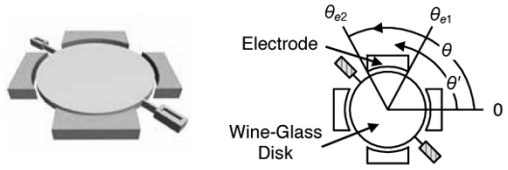
Electrical Equivalent Model	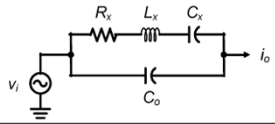	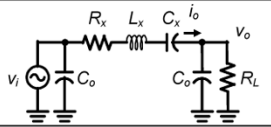
Resonance Frequency	$f_o = 1.03 \cdot \kappa \cdot \sqrt{\frac{E}{\rho}} \cdot \frac{h}{L_r^2} \cdot \left[1 - \left(\frac{k_e}{k_m}\right)\right]^{1/2}$ (T1.1) $\frac{k_e}{k_m} = \int_{L_{e1}}^{L_{e2}} \frac{V_P^2 \varepsilon_o W_r}{[d(y)]^3 k_m(y)} dy$ $L_{e1} = 0.5(L_r - W_e)$, $L_{e2} = 0.5(L_r - W_e)$ (T1.2)	$\left[\Psi_n\left(\frac{\zeta}{\xi}\right) - n - q\right] \cdot [\Psi_n(\zeta) - n - q] = (nq - n)^2$ (T1.3) $\Psi_n(x) = \frac{xJ_{n-1}(x)}{J_n(x)}$, $q = \frac{\zeta^2}{2n^2 - 2}$, $\zeta = 2\pi f_o R\sqrt{\frac{\rho(2+2\sigma)}{E}}$, $\xi = \sqrt{\frac{2}{1-\sigma}}$, $n = 2$ (T1.4) Here, $k_e << k_m$, so k_e is neglected.
Effective Mass	$m_r(y) = \frac{\rho W_r h \int_0^{L_r} [X_{mode}(y')]^2 (dy')}{[X_{mode}(y)]^2}$ (T1.5) $X_{mode}(y) = \zeta(\cos ky - \cosh ky) + (\sin ky - \sinh ky)$ (T1.6) X_{mode} is the vibration mode shape $k = 4.730/L_r$, $\zeta = -1.01781$ for fundamental mode	$m_r(R,\theta) = \frac{\rho h \int_0^{2\pi} \int_0^R [R_{mode}(r,\theta)]^2 r dr d\theta}{[R_{mode}(R,\theta)]^2}$ (T1.7) $R_{mode}(r,\theta) = \left[\frac{\partial}{\partial r} J_n\left(\frac{\zeta}{\xi R} r\right) + \frac{2B}{A} \frac{1}{r} J_n\left(\frac{\zeta}{R} r\right)\right] \cos n\theta$ (T1.8) R_{mode} is the vibration mode shape $n = 2$, $B/A = -4.5236$ for wine-glass mode
Effective Stiffness	$k_r = k_m - k_e$, $k_r(y) = \omega_o^2 \cdot m_r(y)$ (T1.9) $k_{re} = k_r(L_r/2)$ (T1.10)	$k_r = k_m - k_e \cong k_m$, $k_r(R,\theta) = \omega_o^2 \cdot m_r(R,\theta)$ (T1.11) $k_{re} = k_r(R,0)$ (T1.12)
$\frac{\partial C}{\partial x}, \frac{\partial C}{\partial r}$	$\frac{\partial C}{\partial x} = -\sqrt{\int_{L_{e1}}^{L_{e2}} \int_{L_{e1}}^{L_{e2}} \frac{(\varepsilon_o W_r)^2}{[d(y')d(y)]^2} \frac{k_{re}}{k_r(y')} \frac{X_{mode}(y)}{X_{mode}(y')} dy' dy}$ (T1.13)	$\frac{\partial C}{\partial r} = \sqrt{\int_{\theta_{e1}}^{\theta_{e2}} \int_{\theta_{e1}}^{\theta_{e2}} \frac{(\varepsilon_o h R)^2}{[d(\theta')d(\theta)]^2} \frac{k_{re}}{k_r(R,\theta')} \frac{R_{mode}(R,\theta)}{R_{mode}(R,\theta')} d\theta' d\theta}$ (T1.14)
Output Current	$i_o = V_P \cdot \left\lvert\frac{\partial C}{\partial x}\right\rvert \cdot \frac{\partial x}{\partial t}$ (T1.15)	$i_o = 2 \cdot V_P \cdot \frac{\partial C}{\partial r} \cdot \frac{\partial r}{\partial t}$ (T1.16)
Motional Resistance	$R_x = \frac{\sqrt{k_r m_r}}{Q\eta^2}$, $\eta = V_P \left\lvert\frac{\partial C}{\partial x}\right\rvert$ (T1.17)	$R_x = \frac{\sqrt{k_r m_r}}{Q\eta^2}$, $\eta = V_P \frac{\partial C}{\partial r}$ (T1.18)

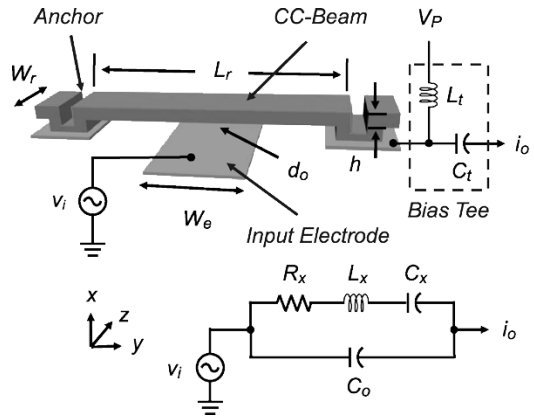

Fig. 2. Perspective view schematic and equivalent circuit of a CC-beam micromechanical resonator under a one-port bias and excitation scheme.

is the radian resonance frequency, all other variables are specified in Fig. 2, and an approximate form for $\partial C/\partial x$ has been used (with the more accurate, but cumbersome, form given in Table I). As the frequency of v_i varies through the beam resonance frequency, the output motional current magnitude i_o traces out a bandpass biquad frequency spectrum identical to that exhibited by an *LCR* circuit, but with a much higher Q than normally achievable by room temperature electrical circuits. Fig. 3 presents the SEM and measured frequency characteristic (under vacuum) for an 8-μm-wide, 20-μm-wide-electrode, 10-MHz CC-beam, showing a measured Q of 3100.

The values of the motional elements in the equivalent circuit of Fig. 2 are governed by the mass and stiffness of the resonator, and by the magnitude of electromechanical coupling at its transducer electrodes. Equations for the elements can be derived by determining the effective impedance seen looking into the resonator port [5], and can be summarized as

$$R_x = \frac{\sqrt{k_r m_r}}{Q\eta^2},\ L_x = \frac{m_r}{\eta^2},\ C_x = \frac{\eta^2}{k_r},\ \eta = V_P \left|\frac{\partial C}{\partial x}\right| \cong V_P \frac{\varepsilon_o A_o}{d_o^2} \quad (6)$$

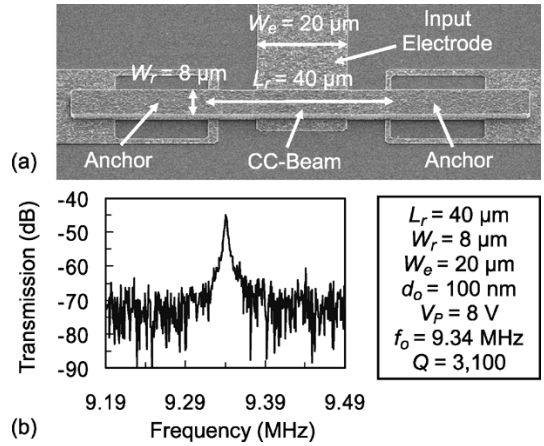

Fig. 3. (a) SEM and (b) frequency characteristic (measured under 20-mtorr vacuum) for a fabricated CC-beam micromechanical resonator with an 8-μm-wide beamwidth and a 20-μm-wide electrode.

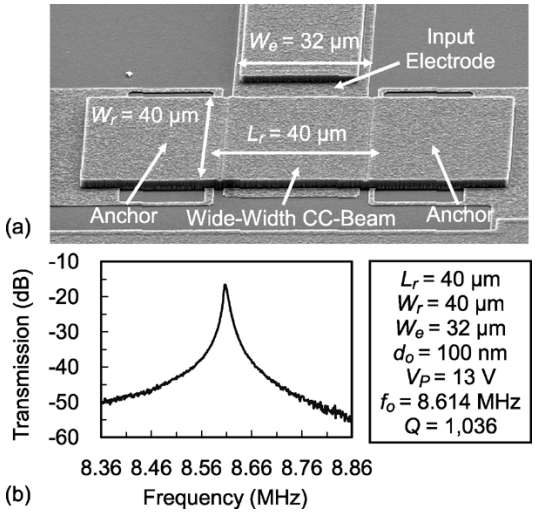

Fig. 4. (a) SEM and (b) frequency characteristic (measured under 20-mtorr vacuum) for a fabricated wide-width CC-beam micromechanical resonator, featuring large beam and electrode widths for lower R_x and higher power-handling ability. Note that the difference in frequency from that of Fig. 3 comes mainly from the larger electrical stiffness caused by a higher dc-bias and a larger electrode-to-beam overlap.

where $k_r = k_m - k_e$ and m_r are the effective stiffness and mass of the resonator beam, respectively, at its midpoint, both given in Table I, and η is the electromechanical coupling factor. The capacitor C_o represents the static overlap capacitance between the input electrode and the structure.

Of the elements in the equivalent circuit, the series motional resistance R_x is perhaps the most important for oscillator design, since it governs the relationship between v_i and i_o at resonance, and thereby directly influences the loop gain of the oscillator system. For the CC-beam resonator of Fig. 2, the expression for R_x can be further specified approximately (neglecting beam bending and distributed stiffness [5]) as

$$R_x = \frac{v_i}{i_o} \cong \frac{k_r}{\omega_o Q V_P^2} \cdot \frac{d_o^4}{\varepsilon_o^2 A_o^2} = \frac{k_r}{\omega_o Q V_P^2} \cdot \frac{d_o^4}{\varepsilon_o^2 W_r^2 W_e^2} \qquad (7)$$

which clearly indicates a strong fourth-power dependence on the electrode-to-resonator gap spacing, as well as a square-law dependence on the dc bias voltage V_P.

As already mentioned, the power-handling ability of a micromechanical resonator greatly influences the phase-noise performance of any oscillator referenced to it. For the case of an oscillator application, the power handling limit of a micromechanical resonator is perhaps best specified by the power running through it when it vibrates at a maximum acceptable amplitude $X_{\max} = ad_o$, which is set either by ALC, or by the pull-in limit (for which $a = 0.56$ at resonance). Using (5) and (7), the maximum power $P_{o\max}$ that a resonator can handle can then be expressed approximately by [22]

$$P_{o\max} = i_o^2 R_x = \frac{\omega_o}{Q} k_r X_{\max}^2 = \frac{\omega_o}{Q} k_r a^2 d_o^2 \qquad (8)$$

where k_r is the effective stiffness of the resonator at its midpoint. Equation (8) asserts that higher power handling can be attained with larger values of stiffness k_r and electrode-to-resonator gap spacing d_o.

The basic CC-beam resonator used in this work is 40 μm long, 2 μm thick, and 8 μm wide, and with these dimensions, can handle a maximum power of only -39.7 dBm ($=0.11$ μW) when $W_e = 20$ μm, $V_P = 8$ V, and $d_o = 100$ nm. In addition, its series motional resistance under these same conditions is 8.27 kΩ, which is quite large compared with the 50 Ω normally exhibited by quartz crystals, and which complicates the design of the sustaining amplifier for an oscillator application.

B. Wide-Width CC-Beam Resonator

One convenient method for reducing R_x and increasing power handling is to widen the width of the CC-beam [11]. For example, the width W_r of the previous CC-beam can be increased from 8 to 40 μm, while also increasing the electrode width W_e from 20 to 32 μm, all without appreciably changing the resonance frequency, which to first order does not depend upon W_r and W_e. Equation (7) predicts that an increase in beamwidth W_r leads to a smaller R_x, mainly due to a larger electrode-to-resonator overlap area that increases electromechanical coupling via the capacitive transducer. This, together with increasing the electrode width W_e to further increase transducer capacitance, comprises the basic strategy used for the wide-width CC-beam to achieve an R_x small enough to allow the use of a single-stage sustaining amplifier (to be described later).

Increasing W_r also seems to lower the Q and increase the effective stiffness k_r of the CC-beam, and according to (7), this reduces the degree to which R_x is lowered. To illustrate, Fig. 4 presents the SEM and measured frequency characteristic (under vacuum) for a 40-μm-wide, 32-μm-wide-electrode 10-MHz CC-beam, showing a Q of 1036, which is 3$\times$ lower than exhibited by previous 8-μm-wide beams. This reduction in Q with increasing beamwidth is believed to arise from increased energy loss through the anchors to the substrate, caused by increases in CC-beam stiffness and in the size of its anchors. A direct consequence of the increase in stiffness, governed by (T 1.5) and (T 1.9), is that the beam pumps harder on its anchors while vibrating, thereby radiating (i.e., losing) more energy per cycle into the substrate. The increase in anchor size further exacerbates this energy loss mechanism by creating a better match

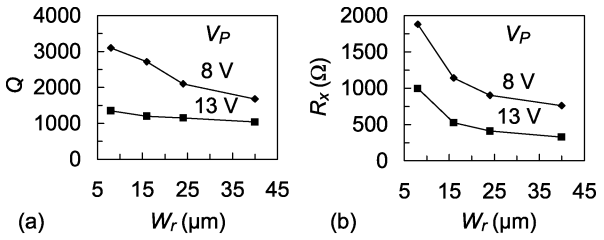

Fig. 5. Measured plots of (a) Q and (b) series motional resistance R_x, versus beamwidth W_r for $V_P = 8$ V and 13 V (where $L_r = 40\ \mu$m, $W_e = 32\ \mu$m, $d_o = 100$ nm are fixed), showing a net decrease in R_x, despite a decrease in Q.

between the resonator and the substrate, allowing for more efficient energy transfer between the two, hence, lower Q.

Fortunately, this decrease in Q is not enough to prevent R_x decrease, and in fact, R_x still decreases as beamwidth increases. Fig. 5(a) and (b) presents measured plots of Q and R_x versus beamwidth W_r, showing that despite reductions in Q, the net effect of beam widening is still a decrease in R_x. In particular, beam widening has reduced the R_x of a CC-beam resonator from the 17.5 kΩ (with $V_P = 7$ V) of the 8-μm-wide device described above [10], to now only 340 Ω (with $V_P = 13$ V), which can be extracted from the height of the frequency spectrum shown in Fig. 4(b). It should also be noted that although the Q of the CC-beam resonator drops from 3100 to 1036 as a result of a wider beamwidth, this Q is still more than two orders of magnitude larger than that achievable by on-chip spiral inductors, and is still suitable for many wireless applications.

In addition to a lower R_x, and perhaps more importantly, the use of a wide-width CC-beam provides the additional advantage of a larger power handling ability, which comes about due to increased stiffness k_r. In particular, the stiffness of the 40-μm-wide beam used here is 9240 N/m, which is 4.97$\times$ larger than the 1860 N/m of the previous 8-μm-wide CC-beam, and which according to (8), when accounting for decreased Q, provides a net 9.06$\times$ higher oscillator output power. For the same $V_P = 8$ V, at which Qs of 3100 and 1700 are exhibited by the 8-μm-wide and 40-μm-wide CC-beams, respectively, this results in a 9.57 dB lower far-from-carrier phase-noise floor for the 40-μm-wide beam.

C. Wine Glass Disk Resonator

Even after widening their beam and electrode widths, the power handling ability of stand-alone CC-beams is still not sufficient for some of the more stringent specifications, such as for the far-from-carrier phase noise in the GSM standard. In addition, for reference oscillator applications, CC-beam micromechanical resonators have a frequency range practically limited to less than 30 MHz, since their Qs drop dramatically as their beam lengths shrink. In particular, the increase in anchor losses with beam stiffness described above become enormous as frequencies rise, to the point where the Q at 70 MHz drops to only 300 [28]. One solution to this problem that retains the simplicity of a beam resonator is to support the beam not at its ends, but at nodal locations, and design the supports so that anchor losses through the supports are minimized when the beam vibrates in a free–free mode shape. Free–free beam micromechanical resonators have been successfully demonstrated, one with a frequency of 92 MHz and a Q of 7450 [29].

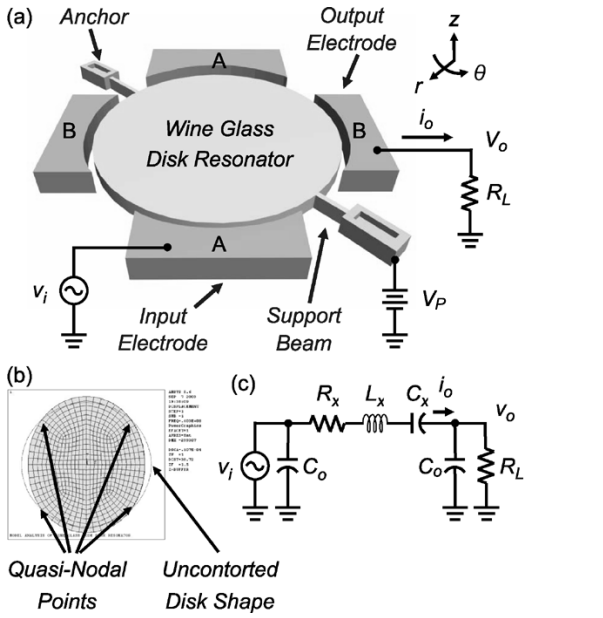

Fig. 6. (a) Perspective-view schematic of a micromechanical wine glass-mode disk resonator in a typical two-port bias and excitation configuration. Here, electrodes labeled A are connected to one another, as are electrodes labeled B. (b) Wine-glass mode shape simulated via finite element analysis (using ANSYS). (c) Equivalent *LCR* circuit model.

Even better performance, however, can be obtained by abandoning the beam geometry and moving to a disk geometry. In particular, radial-mode disk resonators have recently been demonstrated with Qs >10 000 at frequencies exceeding 1.5 GHz, even when operating in air [18]. wine-glass-mode disks have now been demonstrated at 60 MHz with Qs on the order of 145 000 [6], which is the highest yet reported for any on-chip resonator in the frequency range needed for reference oscillators. This, together with the much larger stiffness (hence, higher power handling) of a wine glass disk relative to the beam-based counterparts previously described, inspires the use of a wine glass disk for oscillator applications.

As shown in Fig. 6(a), the wine glass disk resonator of this work consists of a 3-μm-thick disk floating above the substrate, supported by two beams that attach to the disk at quasi-nodal points [6], which have negligible displacement compared to other parts of the disk structure when the disk vibrates in its wine glass mode shape, shown in Fig. 6(b). In this mode shape, the disk expands along one axis and contracts in the orthogonal axis. Four electrodes surround the disk with a lateral electrode-to-disk gap spacing of only 80 nm, made tiny to maximize capacitive transducer coupling governed by η in (6). Opposing electrodes along a given axis are connected in pairs as shown in Fig. 6(a) to affect a drive forcing configuration along the A-axis that compresses and expands the disk with the mode shape of Fig. 6(b), while sensing an oppositely directed motion along the sense axis B. In this configuration, if the A- and B-axis electrodes are identically sized, current entering where the disk compresses (i.e., where $\partial r/\partial t$ in (T 1.16) is negative), leaves where the disk expands (i.e., where $\partial r/\partial t$ in

(T 1.16) is positive), giving this device a pass-through nature at resonance with a 0° phase shift from the A-axis (input) electrode to the B-axis (output) electrode.

The two-port nature of this device whereby the input and output electrodes are physically distinct from the resonator itself further allows a bias and excitation configuration devoid of the bias tee needed in Fig. 2, hence, much more amenable to on-chip integration. In particular, the applied voltages still consist of a dc bias voltage V_P and an ac input signal v_i, but now V_P can be directly applied to the resonator itself without the need for a bias tee to separate ac and dc components. Similar to the CC-beam, these voltages result in a force proportional to the product $V_P v_i$ that drives the resonator into the wine glass vibration mode shape when the frequency of v_i matches the wine glass resonance frequency, given by [30]

$$\left[\Psi_n\left(\frac{\zeta}{\xi}\right) - n - q\right] \cdot [\Psi_n(\zeta) - n - q] = (nq - n)^2 \tag{9}$$

where

$$\begin{aligned} \Psi_n(x) &= \frac{xJ_{n-1}(x)}{J_n(x)} \\ q &= \frac{\zeta^2}{2n^2 - 2} \\ \zeta &= 2\pi f_o R\sqrt{\frac{\rho(2+2\sigma)}{E}} \\ \xi &= \sqrt{\frac{2}{1-\sigma}} \\ n &= 2 \end{aligned} \tag{10}$$

and where $J_n(x)$ is Bessel function of first kind of order n, f_o is the resonance frequency, R is the disk radius, and ρ, σ, and E, are the density, Poisson ratio, and Young's modulus, respectively, of the disk structural material. Although hidden in the precision of (9)'s formulation, the resonance frequency of this wine glass disk is to first order inversely proportional to its radius R. Once vibrating, the dc biased (by V_P) time-varying output electrode-to-resonator capacitors generate output currents governed also by (5) with $\partial C/\partial x$ replaced by $\partial C/\partial r$, and with a frequency response also characteristic of an *LCR* circuit. However, the equivalent circuit for this two-port disk, shown in Fig. 6(c), differs from the one-port circuit of Fig. 2 in that the electrode-to-resonator capacitor C_o no longer connects the input to the output, but is rather now shunted to ground by the dc biased (i.e., ac ground) disk structure. The removal of C_o from the input-to-output feedthrough path is highly advantageous for the series resonant oscillator configuration used in this work, since it better isolates the input from the output, allowing the majority of the current through the device to be filtered by its high Q bandpass biquad transfer function.

Pursuant to attaining a closed form expression for the series motional resistance R_x, the electrode-to-resonator overlap area A_o for each of the two ports of the wine glass disk resonator is πRh, where R and h are the radius and thickness of the disk structure, respectively. Aside from this difference, the approximate expression for R_x takes on a similar form to that of (7), and can be written as

$$R_x = \frac{v_i}{i_o} \cong \frac{k_r}{\omega_o Q V_P^2} \cdot \frac{d_o^4}{\varepsilon_o^2 A_o^2} = \frac{k_r}{\omega_o Q V_P^2} \cdot \frac{d_o^4}{\varepsilon_o^2 \pi^2 R^2 h^2} \tag{11}$$

where k_r is now the effective stiffness of the disk. For a 3-μm-thick, 32-μm-radius version of the disk in Fig. 6, dc biased to $V_P = 12$ V with 80-nm electrode-to-disk gaps and a Q of 48 000, (11) predicts an R_x of 1.46 kΩ, which is quite reasonable for oscillator implementation.

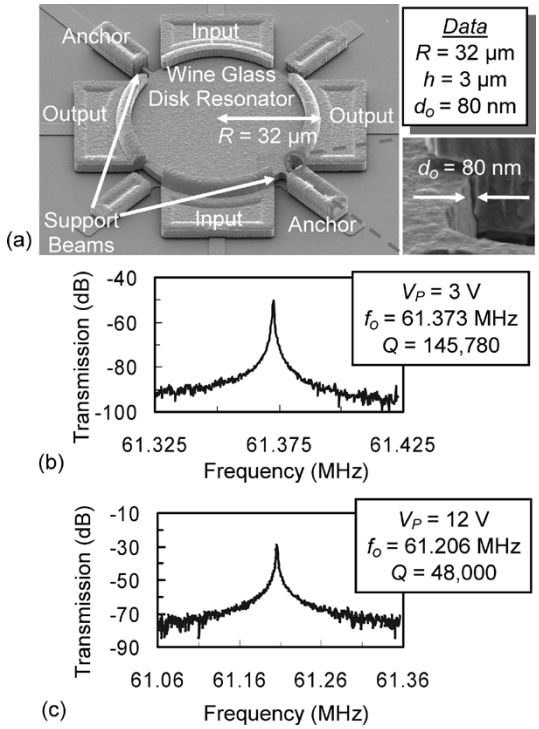

Fig. 7. (a) SEM and (b)–(c) frequency characteristics (measured under 20-mtorr vacuum with different dc bias voltages) of a fabricated 60-MHz wine glass disk resonator with two support beams.

Fig. 7(a) shows the SEM of the fabricated 3-μm-thick, 64-μm-diameter, 60-MHz wine glass disk resonator used in this work, with a zoom-in view of the 80 nm gap after release. Fig. 7(b) and (c) present frequency characteristics measured under a 20-mtorr vacuum, where the device exhibits a Q of 145 780 with $V_P = 3$ V; and 48 000 with $V_P = 12$ V. From the height of the peak of the frequency spectrum in Fig. 7(c), R_x can be extracted to be about 1.5 kΩ, which is very close to the 1.46 kΩ predicted by (11). Although this number is somewhat higher than exhibited by the wide-width CC-beam resonator, it is still quite amenable to many oscillator applications.

The key to achieving improvements on the scale above lies not only in the use of a wine glass disk resonator, but also in the specific advances applied to its design. In particular, the wine glass disk of this work differs from that of a previous prototype [6] in that its thickness h has been increased from 1.5 to 3 μm and gap d_o reduced from 100 to 80 nm in order to increase its power handling and lower its impedance according to (11). In addition, the number of supports used has been reduced from

4 to 2, and the support beamwidth has been reduced from 1.5 μm to 1 μm, all to decrease energy loss from the disk to the substrate through the anchors, and thus, maximize the device Q. Even with these enhancements, the measured R_x of 1.5 kΩ for the 64 μm-diameter 60-MHz wine glass disk with $V_P = 12$ V and $Q = 48\,000$ is still larger than the 50 Ω normally exhibited by off-chip quartz crystals, and thus, in an oscillator application requires a sustaining amplifier capable of supporting higher tank impedance.

With the above modifications, the stiffness of this wine glass disk resonator becomes 6.61×10^5 N/m, which is 71.5$\times$ the 9240 N/m of the previous 10-MHz wide-width CC-beam. Accounting for differences in ω_o, Q, and d_o, (8) predicts a power handling capability 10$\times$ higher for the wine glass disk. For the same $V_P = 8$ V, this should result in a 10-dB lower far-from-carrier phase-noise floor.

IV. Sustaining Amplifier Design

To complete the oscillator circuit, a sustaining amplifier circuit compatible with the comparatively large motional resistance of micromechanical resonators is needed. As mentioned earlier, and as was done with a previous oscillator [21], a transresistance amplifier in series with the resonator is a logical choice, since the low input and output resistances R_i and R_o, respectively, of such an amplifier impose relatively small loading on the resonator, allowing the loaded Q_l of the system to be very close to the large resonator Q, without sacrificing power transfer through the loop. Such an amplifier would need to have sufficient gain, per item 1) of Section II; would need to provide a 0° input-to-output phase shift to accommodate the 0° phase shift of the resonator when operating at series resonance, per item 2) of Section II; and would need to do all of the above with minimal noise and power consumption.

Fig. 8 presents the top-level schematic of the oscillator circuit used in this work, where the micromechanical resonator is represented by its equivalent *LCR* circuit (which in this case assumes the wine glass disk resonator of Fig. 6). As shown, a series resonant configuration is indeed used to best accommodate the medium-range resistance of the micromechanical resonator tanks to be used. However, the particular sustaining amplifier circuit of Fig. 8 differs from previous two-stage circuits [10], [21] not only in its use of only one gain stage, but also in that it achieves the needed 0° phase shift for oscillation in only a single stage, which improves both its noise and bandwidth performance. As shown in the coarse oscillator schematic of Fig. 8, the sustaining circuit is composed of a fully balanced differential CMOS op amp hooked in shunt-shunt feedback on one side, with the output taken from the other. By taking the output from the other side of the differential op amp, an additional 180° phase shift is added on top of the 180° shift from the shunt-shunt feedback, resulting in a total 0° phase shift from input to output, while preserving a low output resistance (due to symmetry) obtained via shunt-shunt feedback. In the detailed circuit schematic of Fig. 9, transistors M_1–M_5 comprise the basic single-stage, differential op amp, while M_{11}–M_{18} constitute a common-mode feedback circuit that sets its output dc bias point. The MOS resistors

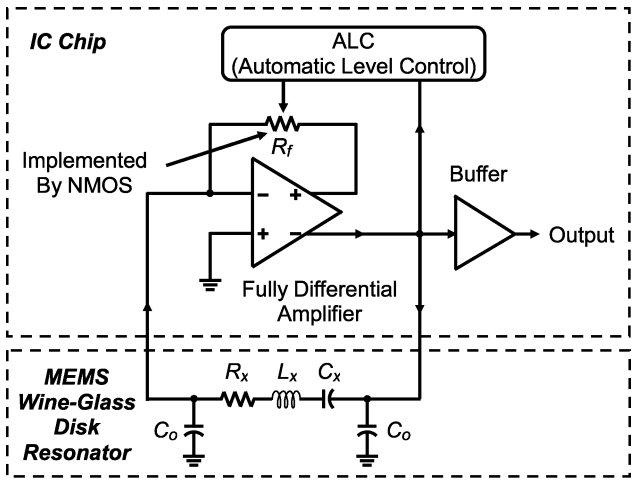

Fig. 8. Top-level circuit schematic of the micromechanical resonator oscillator of this work. Here, the (wine glass disk) micromechanical resonator is represented by its equivalent electrical circuit.

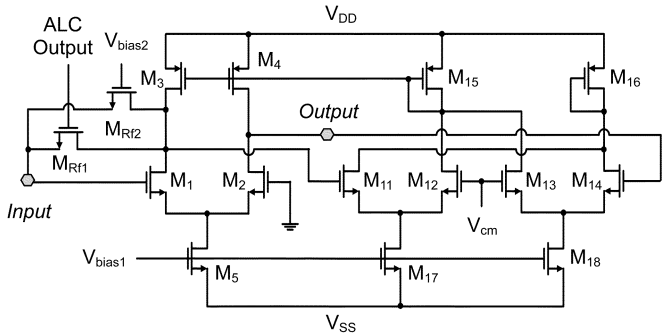

Fig. 9. Detailed circuit schematic of the single-stage sustaining transresistance amplifier of this work, implemented by a fully differential amplifier in a one-sided shunt-shunt feedback configuration.

M_{Rf1} and M_{Rf2} provide resistances R_{Rf1} and R_{Rf2} and serve as shunt-shunt feedback elements that allow control of the transresistance gain via adjustment of their gate voltages. The need for two of them will be covered later in Section V on ALC.

A. Transfer Function

Expressions for the dc transresistance gain, input resistance, and output resistance, of the sustaining amplifier are as follows:

$$R_{\text{amp}} = \frac{\frac{1}{2}g_{m1}(R_f//r_{o1}//r_{o3})R_f}{1+\frac{1}{2}g_{m1}(R_f//r_{o1}//r_{o3})} \cong \frac{g_{m1}R_f^2}{2+g_{m1}R_f} \cong R_f \quad (12)$$

$$R_i = \frac{R_f}{1+\frac{1}{2}g_{m1}(R_f//r_{o1}//r_{o3})} \cong \frac{2R_f}{2+g_{m1}R_f} \cong \frac{2}{g_{m1}} \quad (13)$$

$$R_o = \frac{R_f//r_{o1}//r_{o3}}{1+\frac{1}{2}g_{m1}(R_f//r_{o1}//r_{o3})} \cong \frac{2R_f}{2+g_{m1}R_f} \cong \frac{2}{g_{m1}} \quad (14)$$

where g_{m1} is the transconductance of M_1, r_{o1} and r_{o3} are the output resistance of M_1 and M_3, respectively, R_f is MOS resistor value implemented by M_{Rf1} and M_{Rf2}, assumed to be much smaller than the r_os, and the forms on the far rights assume a large amplifier loop gain $A_l = (1/2)g_{m1}R_f$. (Note that this is amplifier loop gain, not oscillator loop gain.) In practice,

(12)–(14) indicate that $R_{\rm amp}$ depends mainly on R_f, while R_i and R_o depend mainly on the g_m of the input transistors, suggesting that larger input transistor W/L ratios or larger bias currents can further reduce the input and output resistance, hence, reduce Q loading. The latter approach, however, will increase the power consumption of the amplifier and might disturb the impedance balance in the loop.

In addition, the use of larger W/Ls can impact the 3-dB bandwidth of the transresistance amplifier, which as a rule should be at least $10\times$ the oscillation frequency so that its phase shift at this frequency is minimal. In particular, as detailed in [31], an amplifier phase shift close to 0° allows the micromechanical resonator to operate at the point of highest slope in its phase versus frequency curve, which allows it to more effectively suppress frequency deviations caused by amplifier phase deviations. The bandwidth of the transresistance amplifier of Fig. 9 is a function of parasitic capacitance in both the transistors and the micromechanical resonator, and is best specified by the full transfer function for the amplifier

$$R_{\rm amp}(s)=\frac{r_m}{1+r_m\cdot\frac{1}{R_f}}=\frac{R_f\omega_i\omega_b a_v}{s^2+s(\omega_i+\omega_b)+\omega_i\omega_b(1+a_v)} \tag{15}$$

where

$$r_m=\frac{a_v R_f}{\left(1+\frac{s}{\omega_i}\right)\cdot\left(1+\frac{s}{\omega_b}\right)} \tag{16}$$

is the open loop transresistance gain of the base amplifier with feedback loading, where

$$\begin{aligned} a_v &= \frac{1}{2}g_{m1}(R_f//r_{o1}//r_{o3})\cong\frac{1}{2}g_{m1}R_f \\ \omega_i &= \frac{1}{R_f C_{\rm in}} \\ \omega_b &= \frac{1}{(R_f//r_{o1}//r_{o3})C_{\rm out}}\cong\frac{1}{R_f C_{\rm out}} \end{aligned} \tag{17}$$

and where a_v is dc voltage gain of the base op amp, and $C_{\rm in}$ and $C_{\rm out}$ are the total parasitic capacitance at the input and output terminals of the amplifier, respectively, including MOS parasitic capacitance, pad capacitance, and resonator parasitic capacitance. Equation (15) has the form of a lowpass biquad transfer function, with a dc gain $R_{\rm amp}(0)=R_{\rm amp}$ given in (12), and an effective bandwidth given by

$$\omega_{b,eff}\cong\left[\omega_i\omega_b(1+a_v)\right]^{\frac{1}{2}}\cong\left[\frac{2+g_{m1}R_f}{2R_f^2C_{\rm in}C_{\rm out}}\right]^{\frac{1}{2}}. \tag{18}$$

From (18), the bandwidth can be increased by decreasing $C_{\rm in}$ and R_f, and increasing the gain-bandwidth product of the amplifier. For best stability, the effective bandwidth should be chosen to be at least $10\times$ greater than the oscillation frequency. For a given drain current, this places a limit on how large the W/L ratio of the input transistors can be made, since $C_{\rm in}$ grows faster than g_m with increasing W, hence, bandwidth suffers. Bandwidth needs also constrain R_f to a maximum allowable value, while loop gain needs set its minimum value.

B. Sustaining Amplifier Noise

In (2), the phase-noise contribution from the sustaining amplifier is modeled in the noise factor constant $F_{\rm Ramp}$, which can be expanded into

$$F_{\rm Ramp}=\frac{R_{\rm amp}}{R_{\rm noise}} \tag{19}$$

where

$$\frac{1}{R_{\rm noise}}=\frac{\overline{i_{\rm Ramp}^2}}{4kT\Delta f}=\frac{1}{R_f}+\frac{1}{R_f^2}\cdot\frac{\overline{v_{ia}^2}}{4kT\Delta f} \tag{20}$$

where $\overline{i_{\rm Ramp}^2}$ represents the input-referred current noise of the sustaining amplifier, $R_f=(R_{f1}//R_{f2})$, and $\overline{v_{ia}^2}$ is the input-referred voltage noise source of the differential op amp, given by

$$\frac{\overline{v_{ia}^2}}{\Delta f}=4kT\cdot\gamma\cdot\frac{2}{g_{m1}}\cdot\left(1+\frac{g_{m3}}{g_{m1}}\right) \tag{21}$$

where γ is 2/3 for long-channel devices, and from 2–3$\times$ larger for short-channel devices. In (21), all common mode noise sources are nulled by the common-mode feedback circuit. In addition, flicker noise is neglected since the oscillation frequency is beyond the flicker noise corner, and (2) represents only an approximate expression that accounts for $1/f^2$ noise and white noise at large offsets. (If (2) attempted to include $1/f^3$ noise, then transistor flicker noise would need to be included.)

From (21) noise from this sustaining amplifier improves as the size of the op amp input transistors and/or their drain currents increase—the same design changes needed to decrease the amplifier R_i and R_o, with the same bandwidth-based restrictions on input transistor W/Ls. For a given resonator R_x and oscillation frequency f_o, the optimal sustaining amplifier design that still meets wireless handset specifications for the reference oscillator can be found by simultaneous solution of (2), (12), and (18), to obtain the drain current and input transistor Ws that minimize the power consumption.

V. ALC

As will be seen, oscillator limiting via resonator nonlinearity seems to introduce a $1/f^3$ phase-noise component that dominates the close-to-carrier phase noise of micromechanical resonator oscillators [22]. To remedy this, the oscillator IC of this work also includes an ALC circuit, shown in Figs. 8–10, that can insure limiting via electronic methods, rather than by mechanical resonator nonlinearity. This circuit consists of an envelope detector that effectively measures the oscillation amplitude, followed by a comparator that compares the amplitude with a reference value $V_{\rm ref}$, then feeds back a voltage proportional to their difference to the gate of the gain-controlling MOS resistor M_{Rf1} so as to match the oscillation amplitude to $V_{\rm ref}$. In this scheme, since the resistance of M_{Rf1} is very large at the start of oscillation, another MOS resistor M_{Rf2} is placed in parallel with M_{Rf1} and biased to a channel resistance value equal to $3R_{\rm tot}$, which realizes a loop gain greater than 3, and thereby insures oscillation start-up once

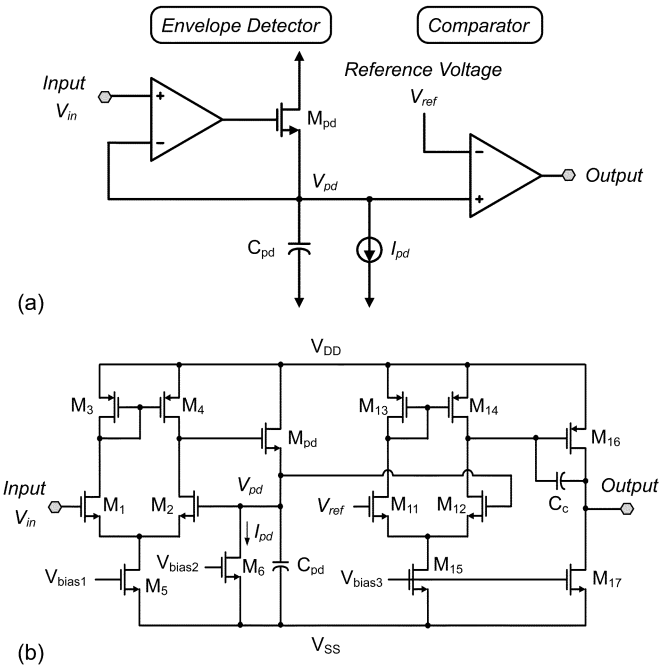

Fig. 10. (a) Top-level and (b) detailed circuit schematics of the ALC circuit.

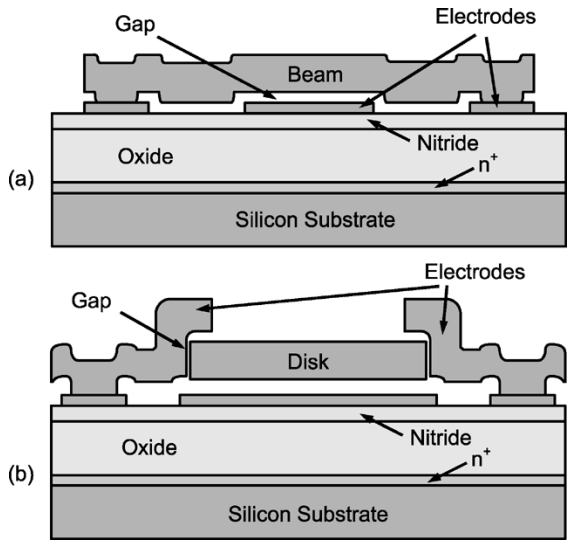

Fig. 11. Final cross-section views of the fabricated (a) CC-beam resonator and (b) wine glass disk resonator.

power is applied. As the amplitude of oscillation grows and the ALC reduces M_{Rf1}'s channel resistance to below that of M_{Rf2}, M_{Rf1} then dictates the total shunt-shunt feedback resistance of the sustaining amplifier.

The envelope detector in Fig. 10 [32] combines a classic op amp-based precision peak rectifier design using an MOS diode $M_{\rm pd}$ in its feedback path, with a capacitive peak sampler $C_{\rm pd}$, and a bleed current source $I_{\rm pd}$ (implemented by M_6) with values of 1 pF and 0.1 μA, respectively, chosen to track an oscillator output with an assumed maximum peak-to-peak variation of 10^5 V/s. In this circuit, when the input voltage $V_{\rm in}$ is larger than the capacitor voltage, $V_{\rm pd}$, $M_{\rm pd}$ is ON and forces $V_{\rm pd}$ to equal to $V_{\rm in}$. On the other hand, when $V_{\rm in} < V_{\rm pd}$, $M_{\rm pd}$ is OFF, allowing $C_{\rm pd}$ to hold $V_{\rm pd}$ against the bleed current of $I_{\rm pd}$, which discharges $C_{\rm pd}$ at the rate of 10^5 V/s.

To attenuate the ripple at the envelope detector output, the bandwidth of the subsequent comparator is purposely limited by implementing it via a two-stage op amp compensated heavily to generate a low frequency dominant pole. A 1-pF compensation capacitor is sufficient to split the poles to 83 kHz and 109 MHz, which provides more than 61° of phase margin, and more importantly, attenuates the 10 MHz ripple by 41.6 dB.

VI. Experimental Results

Standard and wide-width micromechanical CC-beam resonators, such as in Figs. 3 and 4, with cross sections as shown in Fig. 11(a), were fabricated using a small vertical gap polysilicon surface-micromachining process previously used to achieve HF micromechanical filters [5]. Micromechanical wine glass disk resonators, such as in Fig. 7, with cross sections as in Fig. 11(b), were fabricated via a three-polysilicon self-aligned stem process used previously to achieve disk resonators with tiny lateral electrode-to-resonator gaps [6], [17]. Table II summarizes the three resonator designs used in the oscillators of this work.

Fig. 12 presents a photo of the amplifier IC, which was fabricated in TSMC's 0.35-μm process. As shown, the transresistance amplifier lies in the upper mid section, close to the input and output terminals of the chip. The envelope detector and the comparator of the ALC circuit sit adjacent to the amplifier, with their 1-pF capacitors clearly visible. The total IC chip area is about 140 μm $\times$ 100 μm, which together with the 100 μm $\times$ 30 μm required for the CC-beam resonator, the 100 μm $\times$ 60 μm required for the wide-width CC-beam resonator, or the 105 μm $\times$ 105 μm required for the wine glass disk resonator, yields (to the author's knowledge) the smallest footprint to date for any high Q reference oscillator in this frequency range. Tables II and III summarize the design and performance of the overall oscillator circuit.

Interconnections between the IC and MEMS chips were made via wire bonding, and testing was done under vacuum to preserve the high Q of the micromechanical resonators. Fig. 13 presents the measured open-loop gain of the 10-MHz wide-width CC-beam oscillator at various input power levels, showing a spring-softening Duffing nonlinearity that likely contributes to limiting of the oscillation amplitude when the ALC is not engaged. The open loop gain is measured by breaking the oscillator feedback loop at the input electrode of the CC-beam, applying an ac signal to this electrode, and measuring the output power of the transresistance amplifier by directing it through a buffer, then into an HP 4194A Impedance/Gain-Phase Analyzer capable of both forward and reverse frequency sweeps to correctly extract peak values in Duffing-distorted curves. As shown in Fig. 13, as the input power increases, the peaks become smaller, clearly indicating a decrease in open loop gain. Extracting R_x from these peaks and plotting it versus the corresponding input powers yields the curves of Fig. 14, where R_x is seen to increase faster as the input power increases. For this particular resonator, the value of $R_{\rm tot}$ crosses a value equal to the transresistance amplifier gain (set by $R_f = 5$ kΩ), at

TABLE II
RESONATOR DATA SUMMARY

Parameters	10-MHz CC-Beam Resonator	10-MHz Wide-Width CC-Beam Resonator	60-MHz Wine-Glass Disk Resonator	Units
Fabrication Process	Polysilicon-Based Surface Micromachining			—
Young's Modulus, E	150	150	150	GPa
Density, ρ	2,300	2,300	2,300	kg/m^3
Dimensions	Beam Length $L_r = 40$	Beam Length $L_r = 40$	Disk Radius $R = 32$	μm
	Beam Width $W_r = 8$	Beam Width $W_r = 40$		
	Electrode Width $W_e = 20$	Electrode Width $W_e = 32$	Disk Thickness $h = 3$	
	Beam Thickness $h = 2$	Beam Thickness $h = 2$		
Electrode-to-Resonator Gap, d_o	100	100	80	nm
DC-Bias Voltage, V_P	8	13	12	V
Measured Resonant Frequency, f_o	9.34	8.614	61.206	MHz
Measured Quality Factor, Q	3,100	1,036	48,000	—
Effective Mass, m_r	5.86×10^{-13}	2.91×10^{-12}	4.65×10^{-12}	kg
Effective Stiffness, k_r	1.86×10^{3}	8.48×10^{3}	6.61×10^{5}	N/m
Electrode-to-Resonator Overlap Area, A_o	1.6×10^{-10}	1.28×10^{-9}	3.02×10^{-10}	m^2
Measured Equivalent Resistance, R_x	8,790	340	1,500	Ω
Calculated Equivalent Resistance, R_x	8,270	700	1,460	Ω
Calculated Equivalent Inductance, L_x	0.454	0.0134	0.186	H
Calculated Equivalent Capacitance, C_x	0.69	25.59	0.038	fF
Static Overlap Capacitance, C_o	14.17	113.33	33.38	fF
In-Band Power Handling, P_{omax}	-39.7	-28.6	-19.8	dBm
Power Consumption	~ 0	~ 0	~ 0	W
Layout Area	100×30	100×60	105×105	μm^2

TABLE III
OSCILLATOR DATA SUMMARY

Integrated Circuit	Process	TSMC 0.35-μm CMOS
	Voltage Supply	± 1.65 V
	Amplifier Gain	8 kΩ
	Amplifier BW	200 MHz
	Input Resistance	2.1 kΩ
	Output Resistance	2.2 kΩ
	Power Cons. (Amp)	350 μW
	Power Cons. (ALC)	430 μW
	Layout Area	140 μm × 100 μm
10-MHz CC-Beam Resonator Oscillator	Oscillation Power	-42.2 dBm
	Phase Noise @ 1 kHz	-82 dBc/Hz
	Phase Noise @ 10 kHz	-110 dBc/Hz
	Phase Noise @ 100 kHz	-116 dBc/Hz
10-MHz Wide-Width CC-Beam Resonator Oscillator	Oscillation Power	-33.9 dBm
	Phase Noise @ 1 kHz	-80 dBc/Hz
	Phase Noise @ 10 kHz	-106 dBc/Hz
	Phase Noise @ 100 kHz	-120 dBc/Hz
60-MHz Wine-Glass Disk Resonator Oscillator	Oscillation Power	-24.6 dBm
	Phase Noise @ 1 kHz	-110 dBc/Hz
	Phase Noise @ 10 kHz	-128 dBc/Hz
	Phase Noise @ 100 kHz	-132 dBc/Hz
60-MHz ÷ 6 = 10-MHz Wine-Glass Disk Res. Oscillator	Oscillation Power	-24.6 dBm
	Phase Noise @ 1 kHz	-125 dBc/Hz
	Phase Noise @ 10 kHz	-143 dBc/Hz
	Phase Noise @ 100 kHz	-147 dBc/Hz

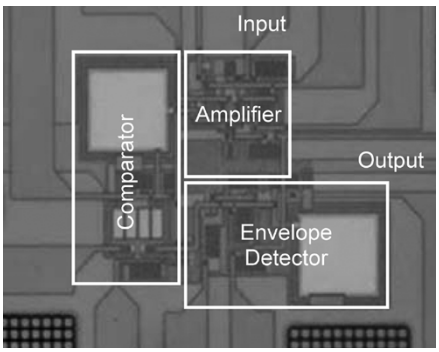

Fig. 12. Photo of the sustaining transresistance amplifier IC fabricated in TSMCs 0.35-μm CMOS process.

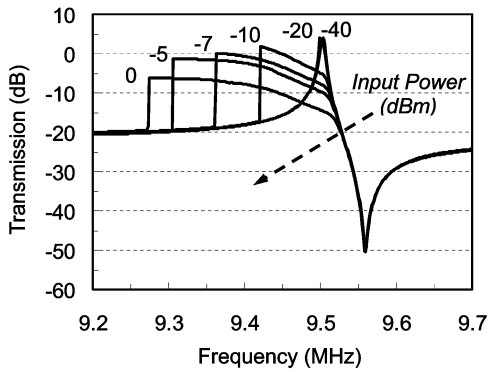

Fig. 13. Measured open-loop gain of the 10-MHz wide-width CC-beam oscillator circuit under increasing input signal amplitudes. These curves were taken via a network analyzer sweeping down in frequency (i.e., from higher to lower frequency along the x-axis).

which point the loop gain of an oscillator would drop to 0 dB, the oscillation amplitude would stop growing, and steady-state oscillation would ensue. Although the plot of Fig. 13 seems to imply that Duffing nonlinearity might be behind motional resistance increases with amplitude, it is more likely that decreases in Q or $\partial C/\partial x$ with amplitude are more responsible [21], since Duffing is a stiffness nonlinearity, and stiffness (like inductance or capacitance) is a nondissipative property.

Oscillators with the ALC loop of Fig. 10 disengaged were tested first. Fig. 15 presents spectrum analyzer plots and oscilloscope waveforms for oscillators with ALC disengaged using each of the three resonator designs summarized in Table I. Fig. 16 presents plots of phase-noise density versus offset from the carrier frequency for each oscillator, measured by directing the output signal of the oscillator into an HP E5500 Phase Noise Measurement System.

A quick comparison of the oscilloscope waveforms of Fig. 15(a)–(c), which shows steady-state oscillation amplitudes of 42 mV, 90 mV, and 200 mV, for the 8-μm-wide 10-MHz CC-beam, the 40-μm-wide 10-MHz CC-beam, and the 60-MHz wine glass disk, respectively, clearly verifies the utility of wide-CC-beam design and the superiority of the

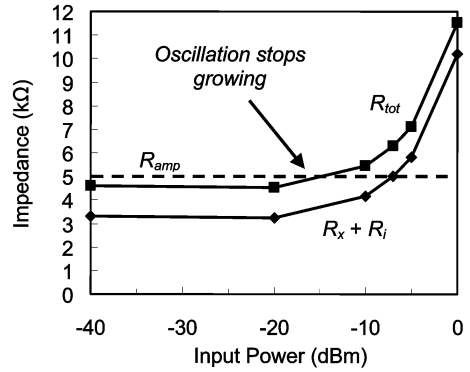

Fig. 14. Extracted R_x from the peaks shown in Fig. 13 versus their corresponding input power. The $R_{\rm tot} = R_x + R_i + R_o$ is also derived from the $R_x + R_i$ curve and compared with $R_{\rm amp}$ for a typical case to illustrate graphical determination of the steady-state oscillation amplitude.

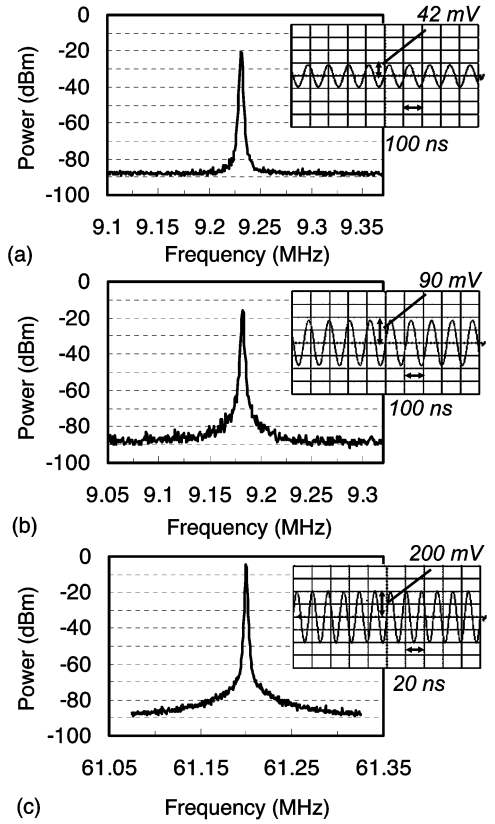

Fig. 15. Measured steady-state Fourier spectra and oscilloscope waveforms for (a) the 10-MHz 8-μm-wide CC-beam resonator oscillator; (b) the 10-MHz 40-μm-wide CC-beam resonator oscillator; and (c) the 60-MHz wine glass disk resonator oscillator. All data in this figure are for the oscillators with ALC disengaged.

wine glass disk design when it comes to power handling. Accounting for the corresponding series motional resistances and output current of each resonator, the corresponding operating powers $P_o = (1/2)(i_o^2 R_{\rm tot})$ for each measured amplitude are 0.061 μW, 0.405 μW, and 3.44 μW. Thus, widening a 10-MHz CC-beam from 8-μm-wide to 40-μm-wide provides a 6.64$\times$ increase in oscillator steady-state power, which is at least consistent with factors given in Section III (but not the same, since the ones in Section III were based on maximum power handling). On the other hand, replacing the wide-width

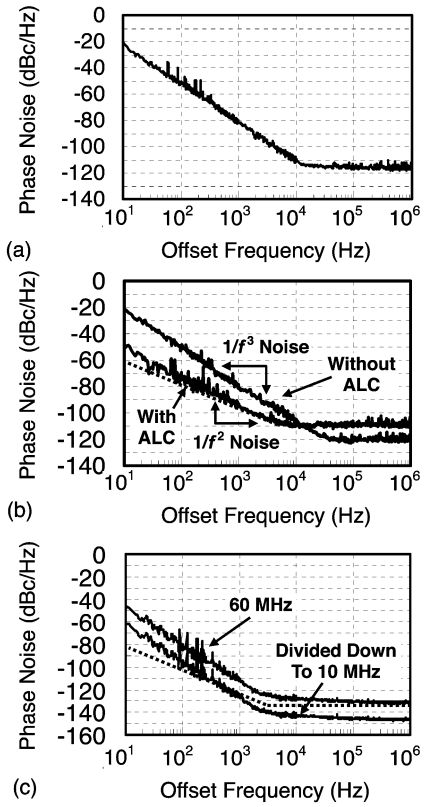

Fig. 16. Phase-noise density versus carrier offset frequency plots for (a) the 10-MHz 8-μm-wide CC-beam resonator oscillator; (b) the 10-MHz 40-μm-wide CC-beam resonator oscillator; and (c) the 60-MHz wine glass disk resonator oscillator. All were measured using an HP E5500 Phase Noise Measurement System. The dotted line is the phase-noise prediction by (2) and (19).

CC-beam entirely by a 60-MHz wine glass resonator yields an 8.49$\times$ increase, again consistent with Section III.

The practical impact of the progressively larger power handlings among the resonators is clearly shown in the phase noise versus carrier offset frequency plots of Fig. 16(a)–(c) for the 8-μm-wide 10-MHz CC-beam, the 40-μm-wide 10-MHz CC-beam, and the 60-MHz wine glass disk, respectively. The far-from-carrier phase-noise levels of -116 dBc/Hz, -120 dBc/Hz, and -132 dBc/Hz, respectively, are close to the predicted values of -118.1 dBc/Hz, -123.6 dBc/Hz, and -134.5 dBc/ Hz, using (2) and (19). For fair comparison, the value for the 60-MHz wine glass disk oscillator becomes -147 dBc/Hz when divided down to 10 MHz, which practically (if not strictly) satisfies the GSM specification.

The close-to-carrier phase noise, on the other hand, looks nothing like the expectation of (2). In particular, rather than the expected $1/f^2$ component, a larger-than-expected $1/f^3$ component is observed that masks the $1/f^2$. The observed $1/f^3$ component is substantially larger than predicted by first-order expressions that assume an aliasing mechanism for $1/f^3$ noise, whereby amplifier $1/f$ noise aliases via micromechanical resonator transducer nonlinearity into the oscillator passband and $1/f^3$ noise is generated via filtering through the resonator transfer function [22]. Other formulations for $1/f^3$ noise based on resonator frequency dependence on the dc bias voltage V_P [22] also do not correctly predict the magnitude of this noise component.

With $1/f^3$ noise dominating, the phase noise for each oscillator at 1-kHz offset from the carrier are -82 dBc/Hz, -80 dBc/Hz, and -110 dBc/Hz, for the 8-μm-wide 10-MHz CC-beam, the 40-μm-wide 10-MHz CC-beam, and the 60-MHz wine glass disk, respectively. For fair comparison, the 1-kHz offset value for the 60-MHz wine glass disk oscillator becomes -125 dBc/Hz when divided down to 10 MHz, which again nearly satisfies the strict GSM specification, and may be close enough regardless.

Although the root of the observed $1/f^3$ phase noise continues to be elusive, a method for removing it is at least available through the ALC loop described in Section V. Fig. 17 presents a measured oscilloscope waveform verifying the functionality of the ALC portion of the oscillator chip when excited by a 10-MHz signal amplitude modulated at 100 kHz used to represent the amplitude variation of the carrier signal. As shown, when the signal amplitude becomes larger than the reference voltage level, the comparator output goes high, which (when the ALC loop is engaged) decreases the value of the MOS resistor M_{Rf1}, reducing the gain of the sustaining amplifier until the loop gain becomes unity, at which point steady-state oscillation ensues.

When the ALC loop is engaged (i.e., connected) for the 10-MHz wide-CC-beam oscillator, the measured phase-noise plot labeled "With ALC" in Fig. 16(b) is observed, where the $1/f^3$ phase noise has disappeared, leaving behind $1/f^2$ phase noise at levels consistent with the prediction of (2). With ALC, this oscillator achieves a close-to-carrier phase noise of -95 dBc/Hz at 1-kHz offset from the 10-MHz carrier, which is an improvement of 15 dB over the oscillator without ALC, and which is now close to the predicted value of -98.9 dBc/Hz using (2) and (19), but which still does not satisfy the GSM specification, since the oscillation amplitude level where $1/f^3$ noise is removed is now only 10 mV. This smaller amplitude is also responsible for the automatic level controlled oscillator having a 10-dB worse phase-noise level of -110 dBc/Hz at far-from-carrier offsets.

Unfortunately, the ALC loop, which was designed specifically for a 10-MHz oscillator, did not function properly when engaged in the 60-MHz wine glass oscillator. It would not be surprising, however, if this oscillator met GSM specifications at 1-kHz offset from the carrier (when divided down to 10 MHz) with the help of ALC. Fabrication of a new oscillator circuit designed to limit the oscillation amplitude of a wine glass disk oscillator is presently underway.

Tables II and III summarize designed and measured results for each oscillator variant, and includes measured power consumption data. For each case, the dc power consumption for the resonator is 0 W, since there is no dc current flowing through the device. This, together with the 350 μW required for the amplifier and 430 μW for the ALC circuit, make this micromechanical reference oscillator suitable for many low power applications.

To better compare the performance of these oscillators with each other and with other existing oscillators, a normalized phase noise has been defined as a figure of merit (FOM) for oscillators [33]:

$$\text{FOM} = L\{f_m\} \cdot \left(\frac{f_m}{f_o}\right)^2 \cdot P_{\text{dis}} \tag{22}$$

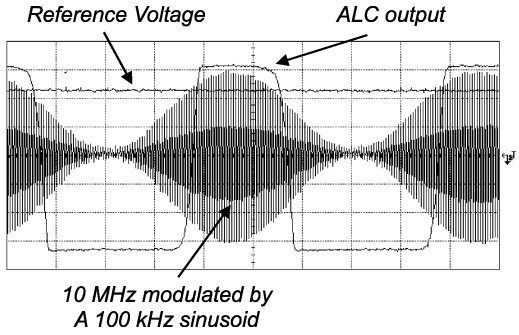

Fig. 17. Measured oscilloscope waveform verifying the functionality of the ALC portion of the oscillator chip when excited by a 10-MHz signal, amplitude modulated at 100 kHz.

where $L\{f_m\}$ is the phase-noise performance of the oscillators (expressed in number, not dB), and P_{dis} is the total oscillator power consumption in milliwatts. For the phase-noise performance of the 60-MHz wine glass disk oscillator, (22) yields a FOM of -210.1 dB at 1-kHz offset. This number is substantially better than -185.5 dB attained by an LC-based VCO [33], and already on par with values achieved by commercial quartz crystal oscillators (-207.2 dB [34] and -211.1 dB [35]). If its $1/f^3$ close-to-carrier phase noise can be removed (as seems feasible with the right kind of amplitude limiting), the micromechanical wine glass disk oscillator of this work is likely to do substantially better than -210.1 dB. Work pursuant to this is ongoing.

VII. Conclusion

Ultrahigh Q oscillators at 10 and 60 MHz have been demonstrated using a hybrid combination of on-chip components, including a custom-designed, single-stage, zero-phase-shift, fully differential amplifier IC together with three different kinds of micromechanical resonators: two 10-MHz CC-beams with varying beamwidths, and a 60-MHz wine glass disk. The 60-MHz wine glass disk oscillator exhibits an oscillator phase noise of -110 dBc/Hz at 1-kHz offset from the carrier, and -132 dBc/Hz at far-from-carrier offsets. Dividing down to 10 MHz for fair comparison, these values equate to -125 dBc/Hz at 1-kHz offset, and -147 dBc/Hz at far-from-carrier offsets which very nearly satisfy the GSM specification for wireless handsets, if not already (for practical purposes). With design improvements to eliminate an unexpected $1/f^3$ phase-noise component, and with design options to increase power handling (including the use of other resonators, such as the extensional wine-glass-mode ring resonator [19]), there seems to be plenty of room for further performance improvement.

References

[1] A. Mason, N. Yazdi, A. V. Chavan, K. Najafi, and K. D. Wise, "A generic multielement microsystem for portable wireless applications (invited)," *Proc. IEEE*, vol. 86, pp. 1733–1746, Aug. 1998.

[2] J. M. Rabaey, J. Ammer, T. Karalar, S. Li, B. Otis, M. Sheets, and T. Tuan, "PicoRadios for wireless sensor networks: the next challenge in ultralow power design," in *Proc. IEEE Int. Solid-State Circuits Conf.*, San Francisco, CA, 2002, pp. 200–201.

[3] C. P. Yue and S. S. Wong, "On-chip spiral inductors with patterned ground shields for Si-based RF ICs," *IEEE J. Solid-State Circuits*, vol. 33, pp. 743–752, May 1998.

[4] C. L. Chua, D. K. Fork, K. V. Schuylenbergh, and J.-P. Lu, "Out-of-plane high-Q inductors on low-resistance silicon," *J. Microelectromechanical Systems*, vol. 12, no. 6, pp. 989–995, Dec. 2003.
[5] F. D. Bannon III, J. R. Clark, and C. T.-C. Nguyen, "High-Q HF microelectromechanical filters," *IEEE J. Solid-State Circuits*, vol. 35, pp. 512–526, Apr. 2000.
[6] M. A. Abdelmoneum, M. U. Demirci, and C. T.-C. Nguyen, "Stemless wine glass-mode disk micromechanical resonators," in *Proc. IEEE Int. Conf. Micro-Electro-Mechanical Systems*, Kyoto, Japan, 2003, pp. 698–701.
[7] R. C. Ruby, P. Bradley, Y. Oshmyansky, A. Chien, and J. D. Larson III, "Thin film bulk wave acoustic resonators (FBAR) for wireless applications," in *Proc. IEEE Int. Ultrasonics Symp.*, Atlanta, GA, 2001, pp. 813–821.
[8] S. Pourkamali and F. Ayazi, "SOI-based HF and VHF single-crystal silicon resonators with sub-100 nanometer vertical capacitive gaps," in *Proc. Int. Conf. Solid-State Sensors, Actuators, and Microsystems*, Boston, MA, 2003, pp. 837–840.
[9] V. Kaajakari, T. Mattila, A. Oja, J. Kiihamäki, H. Kattelus, M. Koskenvuori, P. Rantakari, I. Tittonen, and H. Seppä, "Square-extensional mode single-crystal silicon micromechanical RF-resonator," in *Proc. Int. Conf. Solid-State Sensors, Actuators, and Microsystems*, vol. 2, Boston, MA, 2003, pp. 951–954.
[10] S. Lee, M. U. Demirci, and C. T.-C. Nguyen, "A 10-MHz micromechanical resonator Pierce reference oscillator for communications," in *Proc. Int. Conf. Solid-State Sensors and Actuators*, Munich, Germany, 2001, pp. 1094–1097.
[11] Y.-W. Lin, S. Lee, Z. Ren, and C. T.-C. Nguyen, "Series-resonant micromechanical resonator oscillator," in *Proc. IEEE Int. Electron Devices Meeting*, Washington, DC, 2003, pp. 961–964.
[12] Y.-W. Lin, S. Lee, S.-S. Li, Y. Xie, Z. Ren, and C. T.-C. Nguyen, "60-MHz wine-glass micromechanical-disk reference oscillator," in *Proc. IEEE Int. Solid-State Circuits Conf.*, San Francisco, CA, 2004, pp. 322–323.
[13] B. P. Otis and J. M. Rabaey, "A 300-μW 1.9-GHz CMOS oscillator utilizing micromachined resonators," *IEEE J. Solid-State Circuits*, vol. 38, pp. 1271–1274, July 2003.
[14] V. Kaajakari, T. Mattila, A. Oja, J. Kiihamäki, and H. Seppä, "Square-extensional mode single-crystal silicon micromechanical resonator for low-phase-noise oscillator applications," *IEEE Electron Device Lett.*, vol. 25, pp. 173–175, Apr. 2004.
[15] W.-T. Hsu and C. T.-C. Nguyen, "Stiffness-compensated temperature-insensitive micromechanical resonators," in *Proc. IEEE Int. Conf. Micro-Electro-Mechanical Systems*, Las Vegas, NV, 2002, pp. 731–734.
[16] M. E. Frerking, *Crystal Oscillator Design and Temperature Compensation*. New York: Van Nostrand Reinhold, 1978.
[17] J. Wang, Z. Ren, and C. T.-C. Nguyen, "Self-aligned 1.14-GHz vibrating radial-mode disk resonators," in *Proc. Int. Conf. Solid-State Sensors, Actuators, and Microsystems*, Boston, MA, 2003, pp. 947–950.
[18] J. Wang, J. E. Butler, T. Feygelson, and C. T.-C. Nguyen, "1.51-GHz nanocrystalline diamond micromechanical disk resonator with material-mismatched isolating support," in *Proc. IEEE Int. Conf. Micro-Electro-Mechanical Systems*, Maastricht, The Netherlands, 2004, pp. 641–644.
[19] Y. Xie, S.-S. Li, Y.-W. Lin, Z. Ren, and C. T.-C. Nguyen, "UHF micromechanical extensional wine-glass-mode ring resonators," in *Proc. IEEE Int. Electron Devices Meeting*, Washington, DC, 2003, pp. 953–956.
[20] S.-S. Li, Y.-W. Lin, Y. Xie, Z. Ren, and C. T.-C. Nguyen, "Micromechanical 'hollow-disk' ring resonators," in *Proc. IEEE Int. Conf. Micro-Electro-Mechanical Systems*, Maastricht, The Netherlands, 2004, pp. 821–824.
[21] C. T.-C. Nguyen and R. T. Howe, "An integrated CMOS micromechanical resonator high-Q oscillator," *IEEE J. Solid-State Circuits*, vol. 34, pp. 440–455, Apr. 1999.
[22] S. Lee and C. T.-C. Nguyen, "Influence of automatic level control on micromechanical resonator oscillator phase noise," in *Proc. IEEE Int. Frequency Control Symp.*, Tampa, FL, 2003, pp. 341–349.
[23] A. E. Franke, J. M. Heck, T.-J. King, and R. T. Howe, "Polycrystalline silicon-germanium films for integrated microsystems," *J. Microelectromechanical Systems*, vol. 12, no. 2, pp. 160–171, Apr. 2003.
[24] A.-C. Wong, Y. Xie, and C. T.-C. Nguyen, "A bonded-micro-platform technology for modular merging of RF MEMS and transistor circuits," in *Proc. Int. Conf. Solid-State Sensors and Actuators*, Munich, Germany, 2001, pp. 992–995.
[25] T. A. Core, W. K. Tsang, and S. J. Sherman, "Fabrication technology for an integrated surface-micromachined sensor," *Solid State Technol.*, vol. 28, pp. 39–47, Oct. 1993.
[26] W. P. Robins, *Phase Noise in Signal Sources*. Stevenage, U.K.: Peregrinus, 1982.
[27] D. B. Leeson, "A simple model of feedback oscillator noise spectrum," *Proc. IEEE*, vol. 54, pp. 329–330, Feb. 1966.
[28] A. C. Wong, J. R. Clark, and C. T.-C. Nguyen, "Anneal-activated, tunable, 68 MHz micromechanical filters," in *Proc. Int. Conf. Solid-State Sensors and Actuators*, Sendai, Japan, 1999, pp. 1390–1393.
[29] K. Wang, A.-C. Wong, and C. T.-C. Nguyen, "VHF free-free beam high-Q micromechanical resonators," *J. Microelectromechanical Systems*, vol. 9, no. 3, pp. 347–360, Sept. 2000.
[30] M. Onoe, "Contour vibrations of isotropic circular plates," *J. Acoust. Soc. Amer.*, vol. 28, no. 6, pp. 1158–1162, Nov. 1956.
[31] C. T.-C. Nguyen, L. P. B. Katehi, and G. M. Rebeiz, "Micromachined devices for wireless communications (invited)," *Proc. IEEE*, vol. 86, pp. 1756–1768, Aug. 1998.
[32] D. A. Johns and K. Martin, *Analog Integrated Circuit Design*. New York: Wiley, 1997, pp. 436–437.
[33] M. Tiebout, "Low-power low-phase-noise differentially tuned quadrature VCO design in standard CMOS," *IEEE J. Solid-State Circuits*, vol. 36, pp. 1018–1024, July 2001.
[34] "DSA322MA TCXO Data Sheet," Daishinku Corporation.
[35] "CVHD-950, ultra-low phase noise voltage controller crystal oscillator data sheet," Crystek Crystals Corporation.

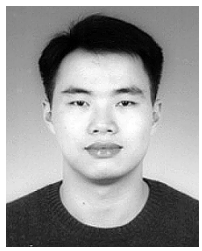

Yu-Wei Lin (S'03) was born in Taipei, Taiwan. He received the B.S. and M.S. degrees in electrical engineering from National Taiwan University, Taipei, Taiwan, in 1997 and 1999, respectively. His master's research involved the design and testing of memory and analog integrated circuits. He is currently working toward the Ph.D. degree in electrical engineering with a major in circuits and microsystems at the University of Michigan, Ann Arbor.

From 1999 to 2001, he served in the Army of the Republic of China as a Second Lieutenant to maintain wireless communications for the military. He is currently working on projects related to micromechanical resonator reference oscillators. His research interests include mixed-signal integrated circuit design and MEMS device fabrication for wireless communication applications.

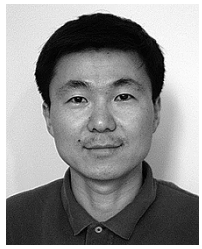

Seungbae Lee (S'01) received the B.S. and M.S. degrees from the Department of Control and Instrumentation Engineering, Seoul National University, Seoul, Korea, in 1990 and 1992, respectively. He is presently working toward the Ph.D. degree in electrical engineering and computer science in the Center for Wireless Integrated Microsystems, University of Michigan, Ann Arbor.

From 1992 to 1997, he was a Senior Research Engineer in LG Electronics Institute of Technology, Seoul, Korea, where he worked on research and development of speech recognition and synthesis. His current research interests focus on microelectromechanical systems for RF wireless communications and include micromechanical resonator reference oscillators and integrated circuit design.

Mr. Lee received the first prize and best paper awards in the Student Design Contest at the 38th Design Automation Conference.

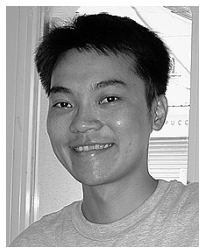

Sheng-Shian Li (S'04) received the B.S. and M.S. degrees in Mechanical Engineering from National Taiwan University, Taipei, Taiwan, in 1996 and 1998, respectively. His M.S. work focused on piezoelectric actuators and nano/micro-positioning systems. He is currently working toward the Ph.D. degree in electrical engineering and computer science with a major in circuits and microsystems from the University of Michigan, Ann Arbor.

From 1998 to 2000, he served in the Republic of China Army as a Second Lieutenant of Brigade Logistics. From 2000 to 2001, he was a Teaching Assistant at National Taiwan University while also conducting research on piezoelectric modal filters. He has been working on projects related to UHF micromechanical resonators and bridged filters.

Yuan Xie (S'03) received the B. S. degree in mechanical engineering from Tsinghua University, Beijing, China, in 1998. He received the M. S. degree in electrical engineering and computer science with a major in circuits and microsystems and a minor in solid-state electronics at the University of Michigan, Ann Arbor, in 2000. He is currently working toward the Ph.D. degree at the University of Michigan.

His research interests focus on the development of UHF micromechanical resonators and filters for wireless communication applications.

Mr. Xie received the Roger A. Haken Best Paper Award at the 2003 IEEE International Electron Devices Meeting.

Zeying Ren (M'04) received the B.S. and M.S. degrees in electrical engineering from Tianjin University, Tianjin, China, in 1987 and 1990, respectively.

From 1990 to 1998, she was a Process Engineer in the National Research Center for Optoelectronics (NCOT), Institute of Semiconductor at the Chinese Academy of Science, Beijing, China. She was a Research Scholar in the Department of Electrical and Computer Engineering, Northwestern University, Evanston, IL, from 1998 to 2000. From 2001 to 2002, she was with Nanovation Technologies as a Process Engineer. In 2002, she joined the Solid State Electronics Laboratory as an Engineer in Research in the Department of Electrical Engineering and Computer Science, University of Michigan, Ann Arbor, where she presently conducts MEMS fabrication.

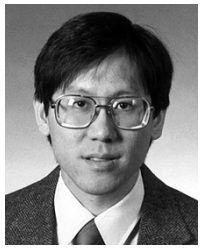

Clark T.-C. Nguyen (S'90–M'95–SM'01) received the B. S., M. S., and Ph.D. degrees from the University of California at Berkeley in 1989, 1991, and 1994, respectively, all in electrical engineering and computer sciences.

In 1995, he joined the faculty of the University of Michigan, Ann Arbor, where he is presently an Associate Professor in the Department of Electrical Engineering and Computer Science. His research interests focus upon microelectromechanical systems (MEMS) and includes integrated micromechanical signal processors and sensors, merged circuit/micromechanical technologies, RF communication architectures, and integrated circuit design and technology. From 1995 to 1997, he was a Member of the National Aeronautics and Space Administration (NASA) New Millennium Integrated Product Development Team on Communications, which roadmapped future communications technologies for NASA use into the turn of the century. In 2001, he founded Discera Inc., a company aimed at commercializing communication products based upon MEMS technology, with an initial focus on the vibrating micromechanical resonators pioneered by his research in past years. He served as Vice President and Chief Technology Officer (CTO) of Discera until mid-2002, at which point he joined the Defense Advanced Research Projects Agency (DARPA) on an IPA, where he is presently the Program Manager of the MEMS, Micro Power Generation (MPG), Chip-Scale Atomic Clock (CSAC), MEMS Exchange (MX), Harsh Environment Robust Micromechanical Technology (HERMIT), Micro Gas Analyzers (MGA), Radio Isotope Micropower Sources (RIMS), and RF MEMS Improvement (RFMIP) programs, in the Microsystems Technology Office of DARPA.

Prof. Nguyen received the 1938E Award for Research and Teaching Excellence from the University of Michigan in 1998, an EECS Departmental Achievement Award in 1999, the Ruth and Joel Spira Award for Teaching Excellence in 2000, and the University of Michigan's 2001 Henry Russel Award. Together with his students, he received the Roger A. Haken Best Student Paper Award at the 1998 and the 2003 IEEE International Electron Devices Meetings, and the Best Frequency Control Student Paper Award at the 2004 IEEE International Ultrasonics, Ferroelectrics, and Frequency Control Symposium.